Available online at www.sciencedirect.com
ScienceDirect
Trans. Nonferrous Met. Soc. China 30(2020) 2915−2926
Transactions of Nonferrous Metals Society of China
www.tnmsc.cn

Microstructure and mechanical properties of Al−Mg−Si alloy U-shaped profile

Xiang-dong WANG[1], Xiong LIU[1], Hao DING[1], Su-rong YAN[1], Zi-hua XIE[1], Bai-qing PAN[1], Yong-hong LI[1], Qing-lin PAN[2], Yun-lai DENG[2], Wei-yi WANG[2]

1. Manufacturing Center, Zhuzhou CRRC Times Electric Co., Ltd., Zhuzhou 412001, China;
2. School of Materials Science and Engineering, Central South University, Changsha 410083, China

Received 19 January 2020; accepted 10 August 2020

Abstract: To get a full understanding of hot extrusion, solid solution treatment and aging process on the Al−0.56Mg−0.63Si alloy, the microstructure and mechanical properties of a U-shaped profile were studied through optical microscopy, scanning electrical microscopy, transmission electrical microscopy, hardness, and tensile tests. The coarse equiaxed grains existed near the profile edge as a result of the dynamic recrystallization nucleation and exceeding growth during hot extrusion. The fibrous deformed and sub-structured grains located between the two coarse grain layers, due to the occurrence of work-hardening and dynamic recovery. Perpendicular needle β'' precipitates were distributed inside the grain, and obvious precipitates-free zone appeared after aging treatment. The tensile strength, yield strength and elongation of the aged Al−Mg−Si alloy U-shaped profile were no less than 279.4 MPa, 258.6 MPa, and 21.6%, respectively. The fracture morphology showed dimple rupture characteristics. The precipitates and grain boundaries played key role in the strengthening contribution.

Key words: Al−Mg−Si alloy; U-shaped profile; hot extrusion; microstructure; mechanical properties; precipitates

1 Introduction

Similar to the automotive industry, steel and aluminum alloys are predominant materials applied in the structural formation of rail trains, including metros, high-speed trains and electric locomotives [1]. Compared with steel, aluminum alloys offer substantial benefits like relative lightness, good manufacturing performance and corrosion resistance. The 5xxx and 6xxx series aluminum alloys are commonly used in sideboards, roof, floor panels and cant rails and the 7xxx series are used for high strength requirements. For example, 5083 and 7N01 aluminum alloys are used in Japan's Shinkansen trains, and 5005 sheets, 6061, 6063 and 6005 extruded profiles are applied in German high-speed rail [2−4].

Al−Mg−Si alloys have moderate strength, good processing formability and fine anti-corrosion [5,6]. However, they face a great challenge in the design and manufacture of differently shaped extrusion profiles since different parts may suffer unequal force, temperature rise and other processing variations [7,8]. A comprehensive understanding of the relationship between mechanical properties and microstructure is essential to ensure the endurance and safety of the extruded profiles. The deformation behaviors in neat-shaped Al−Mg−Si alloy have been systematically studied in the past decade. In the benefit of these simulation tests, most typical deformation characteristics, including dynamic recovery (DRV), dynamic recrystallization (DRX), void formation and cracking, can be determined. SUN et al [9] constructed 3D processing maps to

Corresponding author: Xiang-dong WANG; Tel/Fax: +86-731-28493447; E-mail: Wangxiangdongtimes@163.com
DOI: 10.1016/S1003-6326(20)65431-0

study the hot deformation of 6A02 aluminum alloy and determined that the optimum hot working domains were (450−470 °C, 0.1−1 s^{-1}) and (430−450 °C, 0.01−0.1 s^{-1}). LIU et al [10] studied the hot deformation behaviors of Al−Mg−Si−Mn−Cr alloy through constitutive models and found that lattice diffusion was the dominate mechanism. However, the realistic extrusion of complex shaped profiles in the industry is quite different by considering the fraction and lubrication, the shape and structure of modules [11]. The inhomogeneous deformation and low recrystallization temperature result in the generation of coarse grains, which is not beneficial for the mechanical properties of extrudates [12−14]. For better utilization of these profiles, the mechanical properties and microstructure of complex extruded profiles should be studied.

Heat treatments are efficient ways to improve the mechanical properties of Al−Mg−Si alloys. The generally accepted precipitation sequence during the aging process can be expressed as [15−19]: supersaturated solid solution (SSSS) → clusters → GP zone → β'' precipitates → $\beta'/U_1/U_2/B'$ precipitates → β precipitates. The SSSS formed after solid solution treatment and water quenching. The clusters containing numerous Mg and Si atoms would form in the early stage of aging treatment. The needle-shaped β'' precipitates (Mg_5Si_6) and rod-shaped β' precipitates (Mg_9Si_5) appeared with the prolongation of aging time. Other metastable precipitates like β', U_1 (Al_2MgSi_2), U_2 ($Al_4Mg_4Si_4$), and B' ($Al_3Mg_9Si_7$) could also be detected before the equilibrium β phase formation [20]. However, the characteristics of the precipitates and their effects on the mechanical properties have not been determined.

The objective of this study is to have a full understanding of thermal and mechanical processes on an Al−0.56Mg−0.63Si alloy U-shaped profile. The chemical compositions of different parts were determined by inductively coupled plasma atomic emission spectrometry (ICP-AES). The mechanical properties were determined through hardness tests and room temperature tensile tests. The microstructures were observed by optical microscopy (OM), scanning electron microscopy (SEM) with energy-dispersive spectroscopy (EDS) and electron backscattered diffraction (EBSD), and transmission electron microscopy (TEM). The microstructure evolution during extrusion and the strengthening mechanisms were discussed.

2 Experimental

The chemical composition of the alloy is listed in Table 1, which can be classified as 6005A aluminum alloy [21]. Pure aluminum, magnesium ingots, and Al−Mn, Al−Cr, Al−Cu, Al−Si master alloys were melted in the resistance furnace at about 1023 K. The ingots were cast through semi-continuous casting method. After homogenization at 570 °C for 10 h, the Al−Mg−Si alloy U-shaped profiles were extruded with 4 m/min in temperature range of 460−490 °C, and quenched by water online. The solid solution treatment is (550 °C, 1 h), followed by water quenching to room temperature (25 °C) and the typical aging regime is (175 °C, 10 h). The schematic diagram of the entire extrusion and heat treatment process is shown in Fig. 1.

Table 1 Chemical composition of Al−Mg−Si alloy U-shaped profile (wt.%)

Si	Mg	Fe	Cu	Zn	Cr	Mn	Al
0.628	0.561	0.181	0.022	0.027	0.168	0.232	Bal.

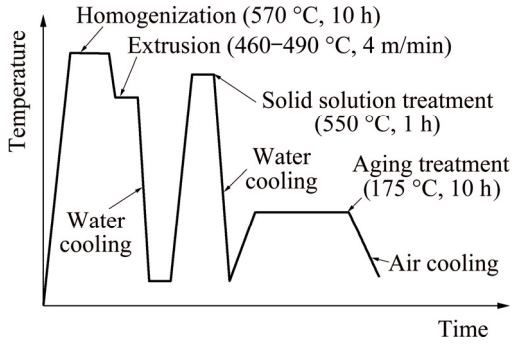

Fig. 1 Schematic diagram of entire extrusion and heat treatment

The microstructures were observed by using an OLYMPUS BX51M (OM), Zeiss M10A (SEM), and TECNAI $G^2$20 (TEM). The OM specimens were mechanically polished and etched with a caustic containing 1% HF, 1.5% HCl and 3% HNO_3. The SEM observation was operated at 20 kV. The statistics of recrystallization fraction was achieved by the recrystallized fraction function in HKL channel 5 software. The filter type is circle, which can distinguish the original large angle grain boundary (>15°) and recrystallized grain boundary (>15°). The deformed and sub-structured grains were low angle grain boundaries, which were lower

than 15°, of which the sub-structured grains were defined as 2°−15° and the deformed grain was below 2°. The TEM samples were sectioned from the middle part of the U-shaped profile, and the TEM observations were carried out at 200 kV. The hardness tests were carried out on the surface of the profile cross- section with loading at 980 N for 15 s and the interval distance of each point was about 5 mm. The room temperature (25 °C) tensile tests were carried out at 2 mm/min. The samples were sectioned along the longitudinal direction of the extruded profile, and the dimensions are shown in Fig. 2. The typical sampling positions are shown as *A* and *B* in Fig. 3.

3 Results

3.1 Microstructure

Figure 3 shows the schematic illustration and OM microstructures at different parts of the

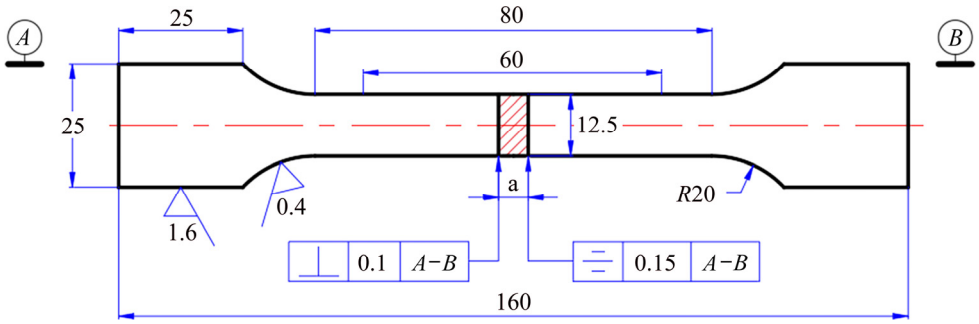

Fig. 2 Dimensions of tensile sample (unit: mm)

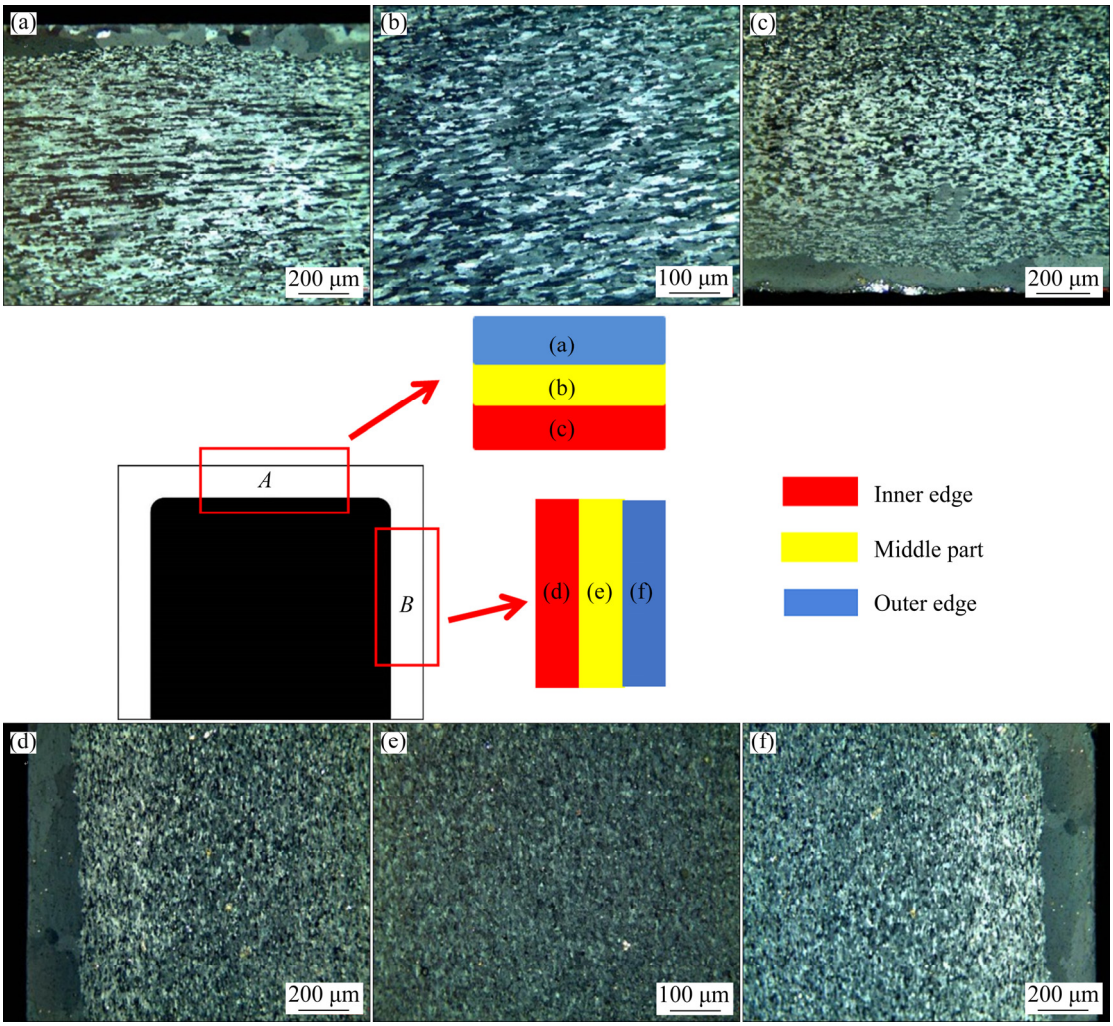

Fig. 3 OM microstructures at different parts of Al−Mg−Si alloy U-shaped profile

Al−Mg−Si alloy U-shaped profile. It presents the multi-layer structure, and the overall thickness is 12 mm. Most grains are in fibrous structure, whereas some coarse equiaxed-grains locate near the profile edge. The thickness of these coarse equiaxed-grains layer at the inner edge is similar to that of the outer edge in Part *A*, which is 50−110 μm. For Part *B*, the thickness is more than 200 μm, which is thicker than that of Part *A*. The grains in both edges contacting with the die experienced complete recrystallization.

Besides, the grain size of those coarse equiaxed grains at the inner edge is smaller than that of the outer edge. The friction between the billet and die induces a great portion of the heat, resulting in the temperature rise in this part. Consequently, it will drive the grain nucleation. The growth and coarsening of nucleated grains lead to the formation of a coarse-grains zone. Generally, the coarse-grains layer is affected by the shape and quantity of the extrusion die hole. For unequal wall profiles, the coarse-grains layer of the thickened section is often deeper than thinner section. In the equal wall profile, the coarse-grain layer may have a similar thickness. The refined grains with recrystallization texture at the edge may have secondary recrystallization, and the grains grow unevenly and rapidly to form coarse grains during subsequent heat treatment. However, those in the middle part are compressed and elongated. Hence, it might consist of deformed and sub-structure grains as a result of deformation and that of DRV.

Figure 4 presents the OM microstructures at the corners (marked by the arrow) of the U-shaped profile. The coarse equiaxed-grains can be observed at the six right-angles and the biggest thickness is about 500 μm. In contrast, the grains of the two R-angles inside the U-shaped profile show a streamlined structure.

The typical SEM images in the given zones of the U-shaped profile are shown in Fig. 5. The corresponding chemical compositions of the relative second phases are listed in Table 2. Generally, numerous secondary particles displayed

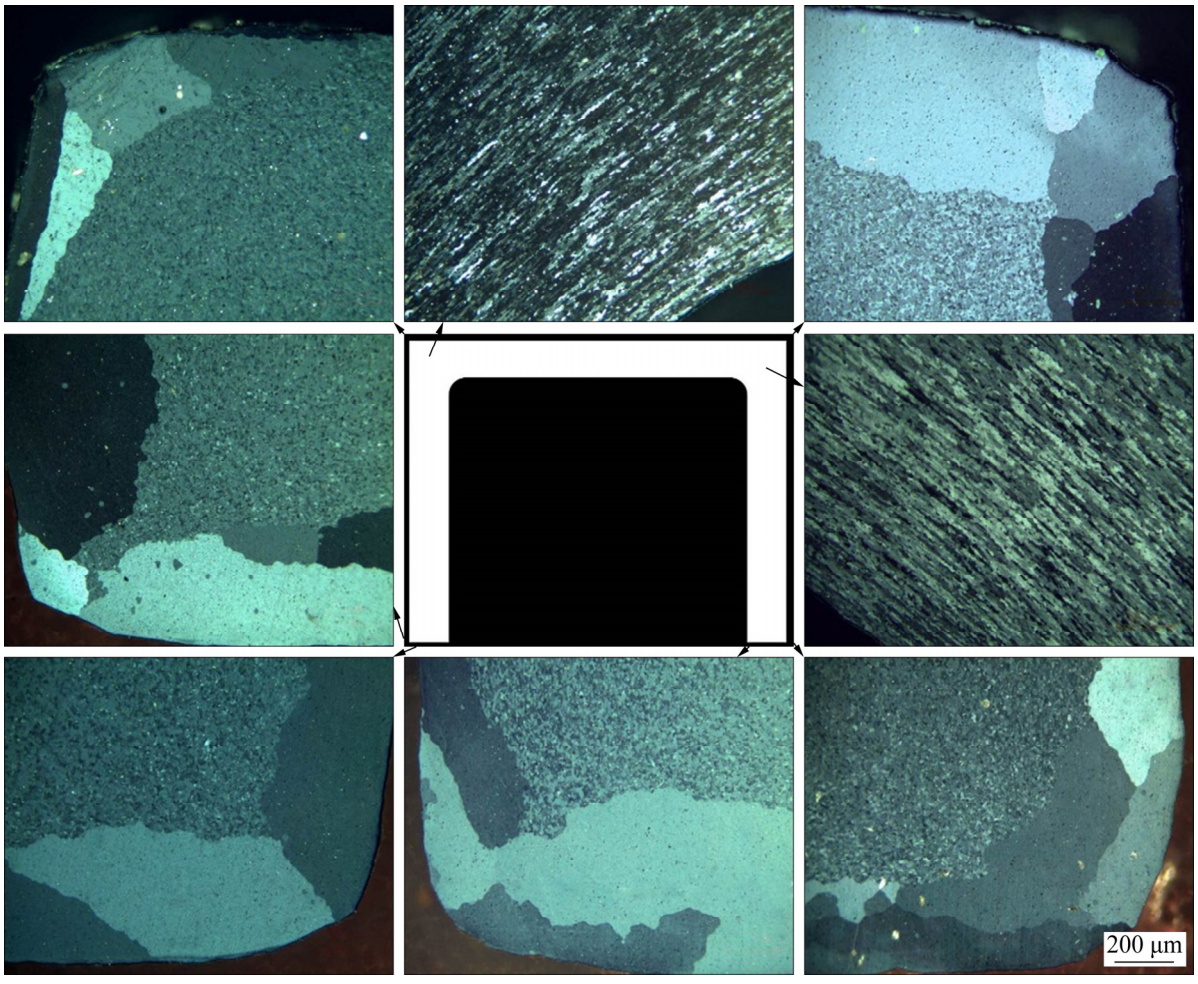

Fig. 4 OM microstructures of Al−Mg−Si alloy U-shaped profile

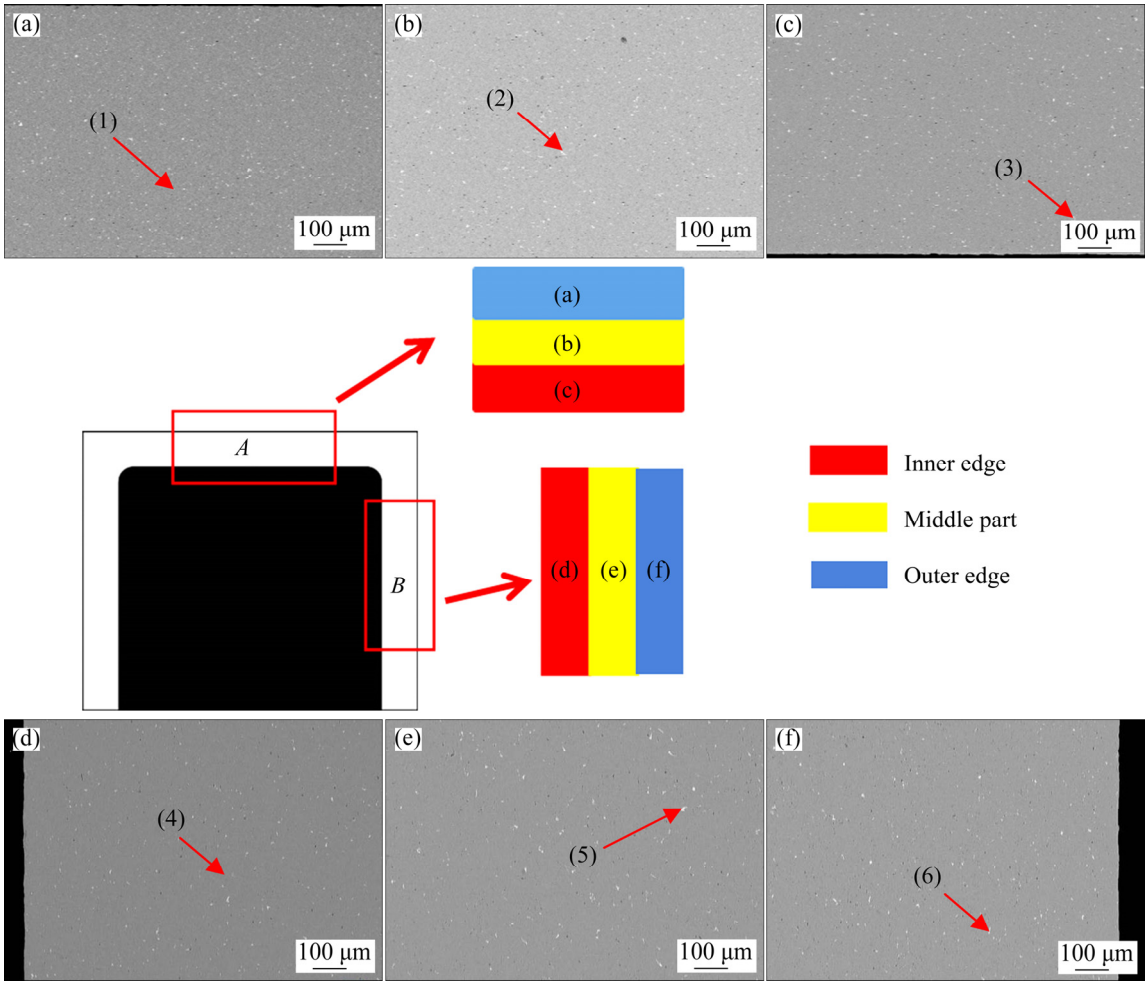

Fig. 5 SEM microstructures in different parts of Al−Mg−Si alloy U-shaped profile

Table 2 Chemical compositions of second phases in marked zones (at.%)

Point	Si	Cr	Mn	Fe	Al
(1)	7.47	1.41	2.73	8.13	80.27
(2)	9.16	2.38	4.35	7.10	77.01
(3)	7.37	0.86	2.87	8.91	79.99
(4)	8.01	1.12	2.87	10.06	77.94
(5)	7.81	1.00	2.62	7.92	80.66
(6)	7.76	1.04	3.13	10.51	77.57

different shapes, including rod, spot or bulk. The sizes of these particles were in the range of 5−15 μm. The white secondary particles contained Mn, Cr, Fe, Si and Al, which might exist as Al(FeCrMn)Si. The low melting point metal, i.e., magnesium, dissolved into the Al matrix and the high melting point metals such as Mn, Cr, Fe, could not diffuse into the matrix during solid solution treatment.

The EBSD images in Parts *A* and *B* of the U-shaped profile in Fig. 3 are displayed in Figs. 6 and 7, respectively. The microstructure presents different characteristics in different zones, classified as the recrystallized, sub-structured and deformed grains. Detailed fractions of the recrystallized, sub-structured and deformed grains are listed in Table 3. For Part *A* (Fig. 6), the recrystallized grains occupy the majority, and the number of deformed grains is the least near the outer edge. The recrystallized grains have obvious abnormal grain growth near the edge. However, the main microstructure is the sub-structured grains in the interior. The amount of deformed grains is the least for both edge and interior zones. For Part *B* (Fig. 7), the grain size in the interior is smaller than that of the outer edge. The main microstructures are recrystallized and sub-structured grains near the edge and in the interior, respectively. This phenomenon indicates no obvious difference between Parts *A* and *B* in this U-shape profile.

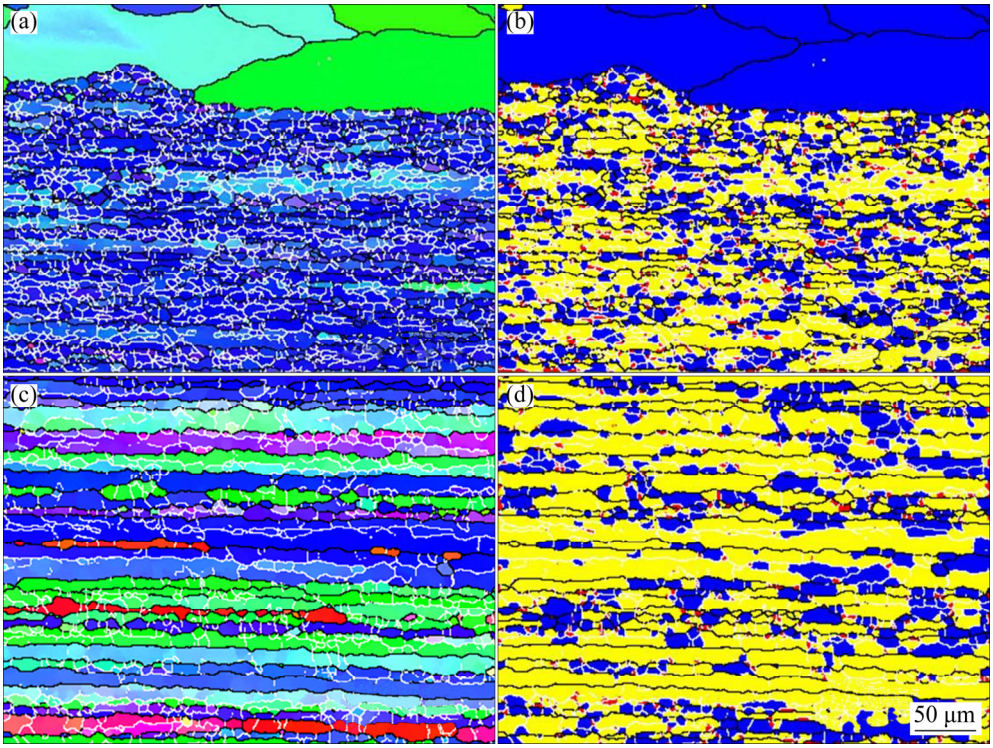

Fig. 6 EBSD images of alloy profile at Part *A* in Fig. 3: (a) IPF microstructure near edge; (b) Recrystallization image near edge; (c) IPF microstructure of interior; (d) Recrystallization image of interior

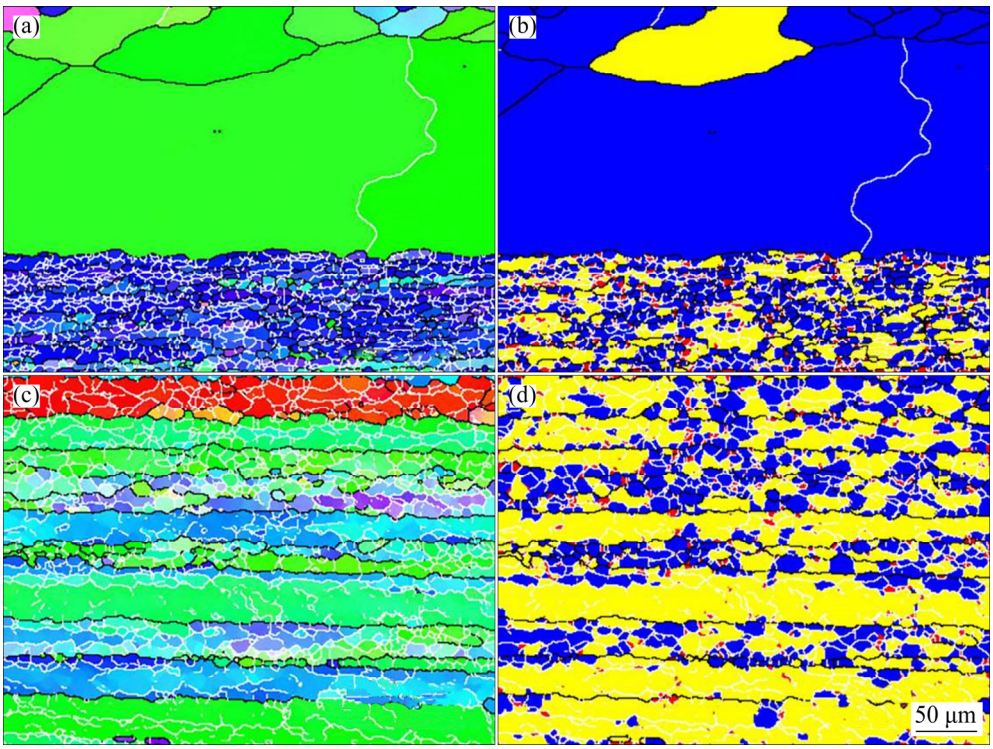

Fig. 7 EBSD images of alloy profile at Part *B* in Fig. 3: (a) IPF microstructure near edge; (b) Recrystallization image near edge; (c) IPF microstructure of interior; (d) Recrystallization image of interior

Figure 8 shows the TEM images along $[100]_{Al}$ axis of this Al−Mg−Si alloy profile. The precipitate-free zone (PFZ) locates along the grain boundary and the width of which is 210 nm, as shown in Fig. 8(a). Large amounts of mutually perpendicular precipitates distribute inside the

Table 3 Percentage of recrystallized, sub-structured and deformed grains

Position	Microstructure	Near edge/%	Inside interior/%
Part *A*	Recrystallized	52.77	26.34
	Sub-structured	40.10	67.29
	Deformed	07.13	04.37
Part *B*	Recrystallized	78.45	33.13
	Sub-structured	16.87	60.87
	Deformed	04.68	06.00

grain, which display needle shape (Fig. 8(b)). The maximum length of the precipitates is around 80 nm. It has been proved by the TEM bright-field images that the transformation of GP zones is completed. Combined with the mechanical properties, the corresponding weak streaks in SAED pattern (red arrows) indicated that the precipitates of the alloy were *β″*. Moreover, some circular precipitates are present in the "intercept" way. The TEM microstructures show similar characteristics in Part *B* (Figs. 8(c, d)). The width of the PFZ is about 280 nm. The mutually perpendicular needle precipitates and circular precipitates exist inside the grain, as shown in Fig. 8(d). The maximum length of the needle precipitates is 100 nm, which is longer than that of Part *A*.

3.2 Mechanical properties

The hardness points of the U-shaped profile are marked with numbers 1−51 in Fig. 9, and the corresponding hardness values are shown in Fig. 10. The distance between each point is 5 mm. The overall hardness values vary from HBW 88.1 to HBW 101.3, with the average at HBW 93.7. The

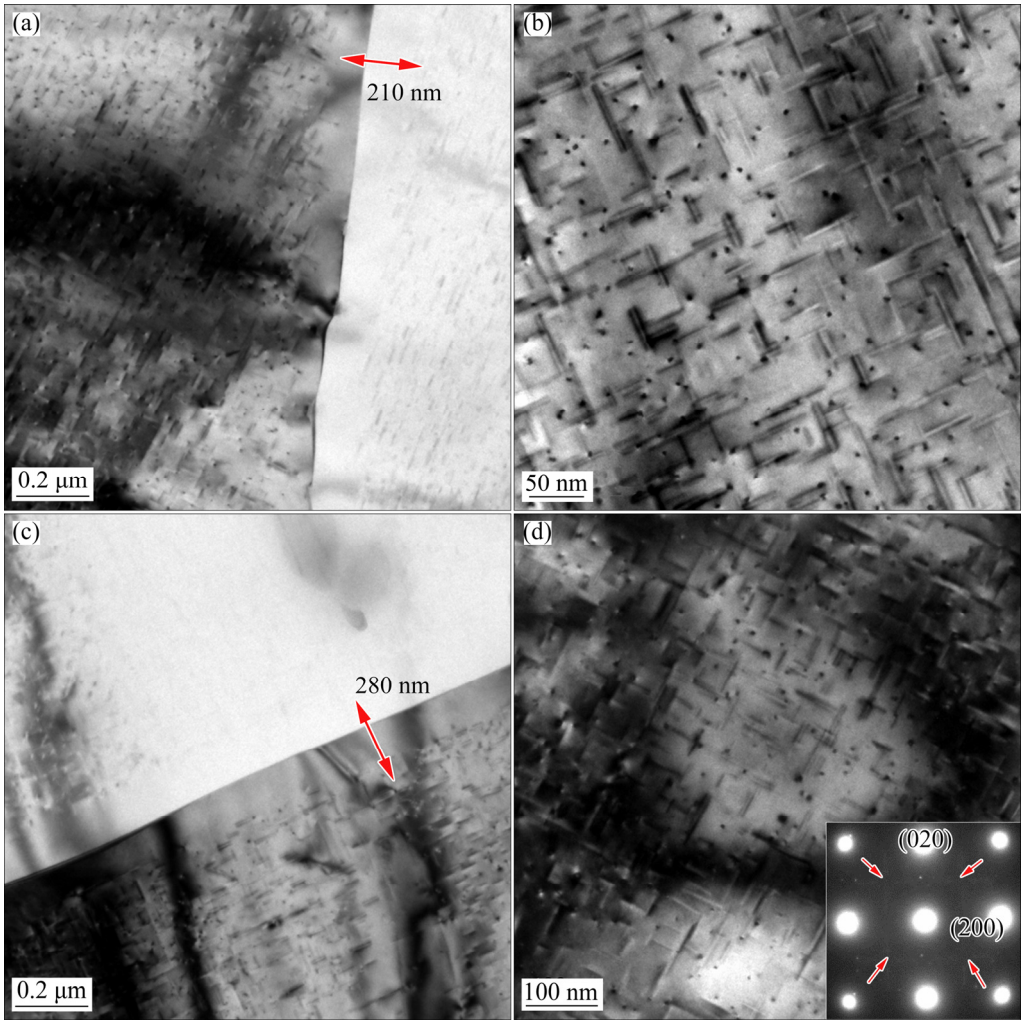

Fig. 8 TEM microstructure and SAED pattern along $[100]_{Al}$ axis of Al−Mg−Si alloy U-shape profile: (a) Grain boundary in Part *A*; (b) Grain interior in Part *A*; (c) Grain boundary in Part *B*; (d) Grain interior and SAED pattern in Part *B*

Fig. 9 Hardness points of Al−Mg−Si alloy U-shaped profile

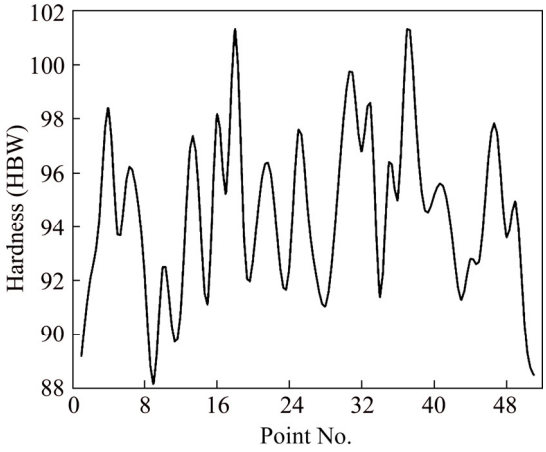

Fig. 10 Hardness values at different points of Al−Mg−Si alloy U-shaped profile

mean hardness value at Part *B* is HBW 93.6 while HBW 94.3 for Part *A*. The mean hardness at the R-angles between Part *A* and Part *B* is HBW 96.8.

The ultimate tensile strength, yield strength and elongation of the U-shaped profile are listed in Table 4. The tensile strength, yield strength and elongation are 283.0 MPa, 262.6 MPa and 21.6% at Part *A*, and 279.4 MPa, 258.6 MPa and 22.3% at Part *B*, respectively. The strength of Part *A* is slightly higher, whereas the elongation is lower than Part *B*. The fracture image presents similar characteristics in both parts. The typical fracture morphologies of various zones in the U-shaped profile are shown in Fig. 11. The fracture images present typical dimple rupture characteristics in different zones.

Table 4 Mechanical properties of different parts in Al−Mg−Si alloy U-shaped profile

Position	R_m/MPa	$R_{p0.2}$/MPa	Elongation/%
Part *A*	283.0	262.6	21.6
Part *B*	279.4	258.6	22.3

4 Discussion

The mechanical properties, including hardness and strength are representatives of microstructure variation in grain size, dislocation, precipitate, and precipitate-free zones (PFZs) of the Al−Mg−Si alloy U-shaped profile, as a consequence of hot extrusion, solid solution and aging treatments. Especially in the process of hot extrusion, various metallurgical phenomena occur, dislocation generation, motion, and annihilation, grain deformation, DRV and DRX. The multi-layer microstructure is composed of coarse equiaxed-grains in the outer edge and inner edge, which are mainly caused by DRX. Large white Al(FeCrMn)Si particles were mainly distributed along the grain boundaries, and perpendicular needle-precipitates existed inside grains. The width of PFZs between two neighbor grains is more than 200 μm. In the interior of the profile, fibrous grains formed by deformation.

ZHANG et al [22] proposed a model to estimate the grain size evolution by combing DRX kinetic model, DRX grain size model and deformed grain size model. The formula of the average grain thickness (d_t)and length (d_l) can be expressed as

$$\begin{cases} d_t = d_{DRX}X_{DRX} + d_{dt}(1-X_{DRX}) \\ d_l = d_{DRX}X_{DRX} + d_{dl}(1-X_{DRX}) \end{cases} \quad (1)$$

where X_{DRX} stands for the fraction of DRX grains, and the expression is represented as

$$X_{DRX} = 1-\exp\left[-k\left(\frac{\varepsilon-\varepsilon_c}{\varepsilon_{ss}}\right)^m\right] \quad (2)$$

where ε_c is the critical strain for the onset of DRX, ε_{ss} is the saturated strain, and k and m are materials constants, respectively. The mean recrystallized grain size can be represented as

$$d_{DRX} = L(T)\ln\dot{\varepsilon} + M(T)\ln\dot{\varepsilon} + N(T) \quad (3)$$

where $L(T)$, $M(T)$ and $N(T)$ are functions of deformation temperature, respectively. Besides, the deformed grain size is determined by combining the experimental observation and numerical simulation. The results showed high consistency in the predicted and realistic grain size.

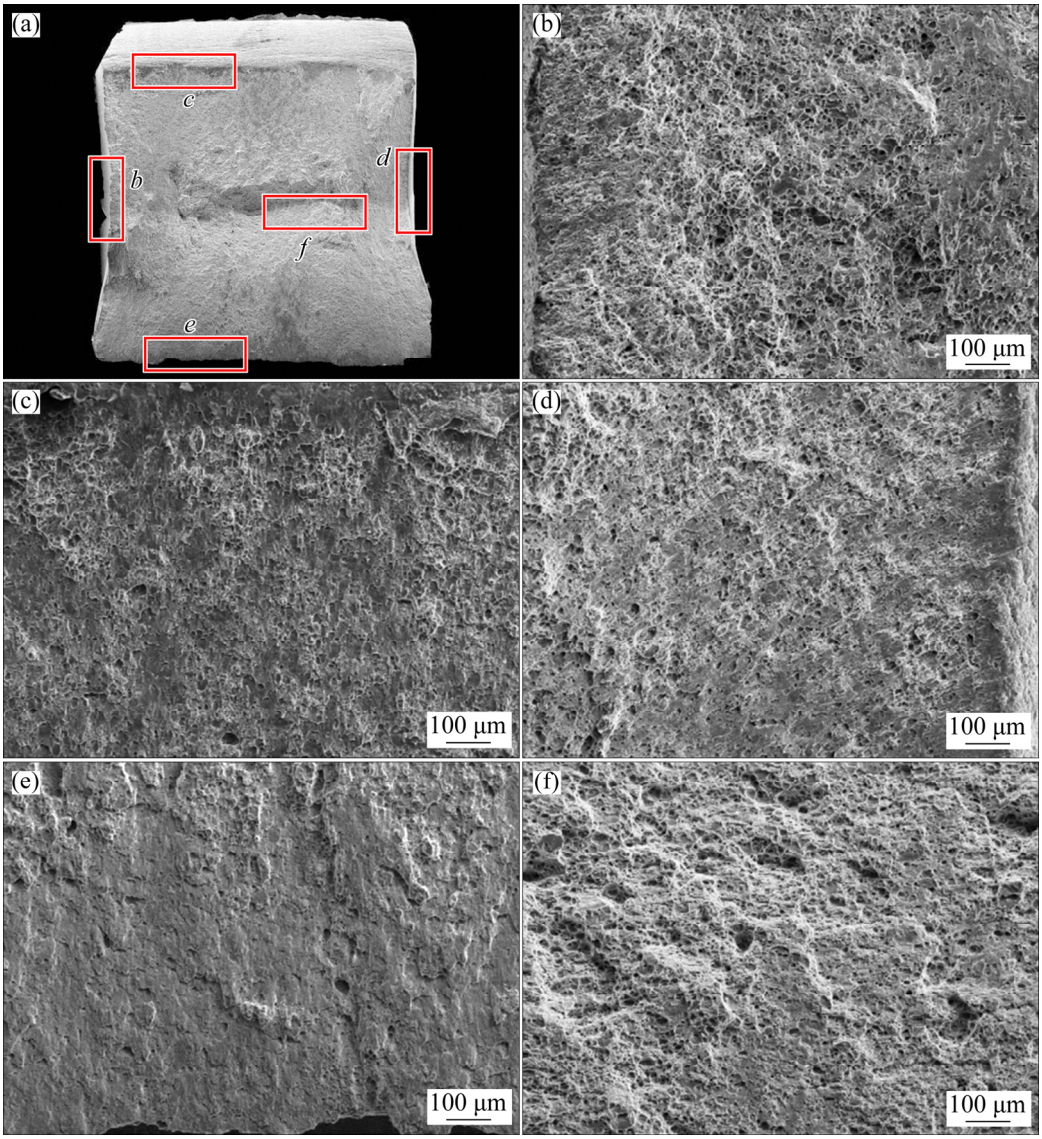

Fig. 11 Typical fracture morphologies of various zones in Al−Mg−Si U-shape profile: (a) Overview; (b) Zone *b*; (c) Zone *c*; (d) Zone *d*; (e) Zone *e*; (f) Zone *f*

In light of this model, the complete vision can be reasonably drawn that the grains between two coarse equiaxed layers of the profile are relatively small. The edge of extrudate originates from the intensive shear zone, and the material of the dead metal zone stays in the die cavity. The velocity of the inner edge and outer edge, including the six right-angles during extrusion, can be treated as almost. The flow rate of two right-angles contacting with the die is low, whereas the strain is high. The middle part in the billet has relatively low strains and comparable velocity to ram speed [23]. The obvious decrease in grain size from the profile edge to the middle part can be attributed to different metallurgical mechanisms. As the strain is induced to the billet, the energy accumulates. As a consequence, the motion of dislocations activates. The mobile dislocations tend to interact with other dislocations in the cells or dislocation walls. When large amounts of dislocations pile up, the sub-grain will form. The well-developed DRV process occurs as a result of high stacking fault energy for aluminum alloy. When the stored energy reaches the maximum, and the dissipation rate decreases to the critical value, the DRX will occur. The temperature rise induced by deformation in the middle part can only trigger partial DRX nucleation. However, the profile edge has a sufficient compact with the die. The temperature increment induced by deformation and fraction leads to the continuous

nucleation of DRX.

The dispersoids and precipitates are also influenced by these thermal and mechanical processes. The Al(MnCrFe)Si dispersoids existed after extrusion and heat treatment, which were usually incoherent with the Al matrix and acted as the heterogeneous nucleation sites for quench-induced precipitates [24,25]. The quench-induced precipitates nucleated preferentially on the Al(MnCrFe)Si dispersoids and grew quickly, the size of which could reach 100 nm. The nucleation, growth and coarsening of these quench-induced precipitates consumed solutes nearby, resulting in the shortage of solutes for Mg_2Si precipitates. Consequently, the PFZ formed in the following aging treatment. However, the Al(MnCrFe)Si dispersoids and the quench-induced precipitates might have a limited strengthening effect. A large amount of the coarse quench-induced precipitates lead to a weak strengthening effect after artificial aging. Besides, Al(MnCrFe)Si dispersoids, grain boundaries and dislocations are preferential nucleation sites for heterogeneous precipitation. The precipitates at grain boundaries might lead to a decrease in the effect of boundary strengthening [26,27]. Meanwhile, the grain boundary precipitates (GBPs) play an essential role in the corrosion behaviors of the profile due to the potential difference between the matrix and the precipitates. The solute migration also contributes to the formation of PFZ during aging treatment. The dislocations are generated and multiplied as a consequence of induced strain during hot extrusion and are still retained in the profile after solid-solution treatment though the quantity decrease. Dislocations are thermodynamically unstable and can be treated as an effective nucleation sites for heterogeneous precipitates of the new phase. After the quench-induced precipitates nucleate around, the missing part of the dislocations releases the corresponding distortion energy, which increases the driving force for nucleation. Meanwhile, solute atoms are often segregated on dislocations, and the dislocations can act as a diffusion channel for solute atom precipitates, which satisfies the requirement of new phase formation [28].

The mechanical properties (tensile strength, yield strength and hardness) are influenced by the microstructures. The effects of coarse equiaxed-grains on tensile properties can be ignored in this U-shaped profile, praised for two reasons. First of all, from the size of the tensile sample, it can be seen that 12 mm is the whole width of the section. The samples must contain coarse equiaxed-grains. However, the width of the coarse equiaxed-grains layer is around 2×200 μm (0.4 mm) in Parts *A* and *B*, as shown in Fig. 3(a). Compared with the total width (12 mm), the effects of coarse equiaxed-grains are negligible. Secondly, coarse equiaxed-grains are located at the edge, and reduced by the grinding process before testing, which can further weaken their influence on tensile properties. The overall strength or hardness is the combination of the Al matrix, dislocations, grain boundaries, solute atoms, dispersoids and precipitates, among which the effects of precipitates and grain boundaries should be more remarkable. The contribution of the solid solution might be low due to the limited solute quantity in the matrix and continuous precipitation during aging. The dislocations would recombine and annihilate during heat treatment processes, and thus, the effect of dislocation strengthening was not counted as the primary factor. The precipitation strengthening and grain boundary strengthening could be interpreted by the Orowan strengthening mechanism and the Hall−Petch effect [29], respectively. The yield strength contributed by precipitates is 112 MPa after solid-solution treatment and aging at 180 °C in an Al−2.08Mg−1.98Si−0.3Mn−0.15Zr−0.1Cr−0.15Ti alloy [30]. For this alloy, precipitation strengthening and grain boundary strengthening might play key roles in the contribution of yield strength.

5 Conclusions

(1) The typical multi-layer structure is shown in the cross-section of the U-shaped profile. The coarse equiaxed-grains existed near the profile edge with a thickness of more than 200 μm. The fibrous deformed and sub-structured grains were present between the two coarse grain layers.

(2) The tensile strength, yield strength and elongation of the profile are no less than 279.4 MPa, 258.6 MPa and 21.6%, respectively. The fracture morphology shows the dimple rupture characteristics.

(3) The strengthening mechanisms were assessed and determined. The β'' precipitates and

grain boundary played key role in the strengthening contribution.

Acknowledgments

The authors want to acknowledge the financial support of project on reliability and life research of typical components in rail trains (K10TZ20P0500) of CRRC Zhuzhou Electric Locomotive Research Institute.

References

[1] ZENG Dong-fang, LU Lian-tao, GONG Yan-hua, ZHANG Ning, GONG Yu-bin. Optimization of strength and toughness of railway wheel steel by alloy design [J]. Materials & Design, 2016, 92: 998−1006.

[2] YAN Jie, PAN Qing-lin, LI An-de, SONG Wen-bo. Flow behavior of Al−6.2Zn−0.70Mg−0.30Mn−0.17Zr alloy during hot compressive deformation based on Arrhenius and ANN models [J]. Transactions of Nonferrous Metals Society of China, 2017, 27: 638−647.

[3] DAI Qing-song, DENG Yun-lai, TANG Jian-guo, WANG Ying. Deformation characteristics and strain-compensated constitutive equation for AA5083 aluminum alloy under hot compression[J]. Transactions of Nonferrous Metals Society of China, 2019, 29: 2252−2261.

[4] SAJU T P, NARAYANAN R G. Effect of tool plunge depth on joint formation and mechanical performance of friction stir forming joints made between AA 5052-H32 and AA 6061-T6 sheet metals [J]. Transactions of Nonferrous Metals Society of China, 2018, 28: 613−628.

[5] ZHANG Cun-sheng, WANG Cui-xue, ZHANG Qing-you, ZHAO Guo-qun, CHEN Liang. Influence of extrusion parameters on microstructure, texture, and second-phase particles in an Al−Mg−Si alloy [J]. Journal of Materials Processing Technology, 2019, 270: 323−334.

[6] ORTIZ J L , CARPIO J J , AMIGO V, SALVADO M D. Pitting corrosion of an Al−Mg−Si−Cu alloy reinforced with nitride particles, P/M processed [J]. Journal of Materials Science Letters, 2001, 20: 197−199.

[7] LI Shi-kang, LI Luo-xing, HE Hong, LIU Zhi-wen, ZHANG Long. Influence of dynamic recrystallization on microstructure and mechanical properties of welding zone in Al−Mg−Si aluminum profile during porthole die extrusion [J]. Transactions of Nonferrous Metals Society of China, 2019, 29: 1803−1815.

[8] YI Jie, WANG Zhen-hu, LIU Zhi-wen, ZHANG Jian-ming, HE Xin. FE analysis of extrusion defect and optimization of metal flow in porthole die for complex hollow aluminium profile [J]. Transactions of Nonferrous Metals Society of China, 2018, 28: 2094−2101.

[9] SUN Yu, CAO Zhuo-han, WAN Zhi-peng, HU Lian-xi, YE Wen-hong, LI Nian-kui, FAN Chang-long. 3D processing map and hot deformation behavior of 6A02 aluminum alloy [J]. Journal of Alloys and Compounds, 2018, 742: 356−368.

[10] LIU Shu-hui, PAN Qing-lin, LI Meng-jia, WANG Xiang-dong, HE Xin, LI Xin-yu, PENG Zhuo-wei, LAI Jian-ping. Microstructure evolution and physical-based diffusion constitutive analysis of Al−Mg−Si alloy during hot deformation [J]. Materials & Design, 2019, 184: 1−15.

[11] YANG Qun-ying, YANG Dong, ZHANG Zhi-qing, CAO Ling-fei, WU Xiao-dong, HUANG Guang-jie, LIU Qing. Flow behavior and microstructure evolution of 6A82 aluminium alloy with high copper content during hot compression deformation at elevated temperatures [J]. Transactions of Nonferrous Metals Society of China, 2016, 26: 649−657.

[12] van GEERTRUYDEN W H, MISIOLEK W Z, WANG P T. Grain structure evolution in a 6061 aluminum alloy during hot torsion [J]. Materials Science and Engineering A, 2006, 419: 105−114.

[13] TANG Jian-wei, CHEN Liang, ZHAO Guo-qun, ZHANG Cun-sheng, CHU Xing-rong. Formation mechanism and evolution of surface coarse grains on a ZK60 Mg profile extruded by a porthole die [J]. Journal of Materials Science and Technology 2020, 47: 88−102.

[14] WILLIAMSON A, DELPLANQUE J P. Investigation of dynamic abnormal grain growth using the Monte Carlo Potts method [J]. Computational Materials Science, 2016, 124: 114−129.

[15] VISSERS R, HUIS M A V, JANSEN J, ZANDBERGEN H W, MARIOARA C D, ANDERSON S J. The crystal structure of the β' phase in Al−Mg−Si alloys [J]. Acta Materialia, 2007, 55: 3815−3823.

[16] EDWARDS G A, STILLER K, DUNLOP G L, COUPER M J. The precipitation sequence in Al−Mg−Si alloys [J]. Acta Materialia, 1998, 46: 3893−3904.

[17] MEYRUEY G, MASSARDIER V, LEFEBVRE W, PEREZ M. Over-ageing of an Al−Mg−Si alloy with silicon excess [J]. Materials Science and Engineering A, 2018, 730: 92−105.

[18] CHEN Liang, YUAN Sheng-wei, KONG De-min, ZHAO Guo-qun, HE Yu-qing, ZHANG Cun-sheng. Influence of aging treatment on the microstructure, mechanical properties and anisotropy of hot extruded Al−Mg−Si plate [J]. Materials & Design 2019, 182: 107999.

[19] TANG Jian-wei, CHEN Liang, ZHAO Guo-qun, ZHANG Cun-sheng, YU Jun-quan, Study on Al/Mg/Al sheet fabricated by combination of porthole die co-extrusion and subsequent hot rolling [J]. Journal of Alloys and Compounds, 2019, 784: 727−738.

[20] CHEN Hai-lin, CHEN Qing, BRATBERG J, ENGSTROM A. Predictions of stable and metastable phase formations in aluminum alloys [J]. Materials Today: Proceedings, 2015, 2: 4939−4948.

[21] SIMAR A, BRECHET Y, MEESTER B, DENQUIN A, PARDOEN T. Sequential modeling of local precipitation, strength and strain hardening in friction stir welds of an aluminum alloy 6005A-T6 [J]. Acta Materialia, 2007, 55: 6133−6143.

[22] ZHANG Cun-sheng, WANG Cui-xue, ZHANG Qing-you, ZHAO Guo-qun, CHEN Liang, SUN Wen-chao, WANG Xie-bin. Investigation of dynamic recrystallization and modeling of microstructure evolution of an Al−Mg−Si aluminum alloy during high-temperature deformation [J]. Journal of Alloys and Compounds, 2019, 773: 59−70.

[23] SCHIKORRA M, DONATI L, TOMESANI L, TEKKAYA A E. Microstructure analysis of aluminum extrusion: Prediction of microstructure on AA6060 alloy [J]. Journal of Materials Processing Technology, 2008, 201: 156−162.
[24] LIU C L, DU Q, PARSON N C, POOLE W J. The interaction between Mn and Fe on the precipitation of Mn/Fe dispersoids in Al−Mg−Si−Mn−Fe alloys [J]. Scripta Materialia, 2018, 152: 59−63.
[25] POLETTI C, WOJCIK T, SOMMITSCH C. Hot deformation of AA6082 containing fine intermetallic particles [J]. Metallurgical and Materials Transactions A, 2012, 44: 1577−1586.
[26] ZHAO Kuo, LIU Jian-hua, YU Mei, LI Song-mei. Through-thickness inhomogeneity of precipitate distribution and pitting corrosion behavior of Al−Li alloy thick plate [J]. Transactions of Nonferrous Metals Society of China, 2019, 29: 1793−1802.
[27] STEELE D, EVENS D, NOLAN P, LLOYD D J. Quantification of grain boundary precipitation and the influence of quench rate in 6XXX aluminum alloys [J]. Materials Characterization, 2007, 58: 40−45.
[28] GARRIC V, COLAS K, DONNADIEU P, RENOU G, URVOY S, KAPUSTA B. Correlation between quenching rate, mechanical properties and microstructure in thick sections of Al Mg Si(Cu) alloys [J]. Materials Science and Engineering A, 2019, 753: 253−261.
[29] WANG Xiang-dong, PAN Qing-lin, LIU LI-li XIONG Shang-wu, WANG Wei-yi. LAI Jian-ping, SUN Yuan-wei, HUANG Zhi-qi. Characterization of hot extrusion and heat treatment on mechanical properties in a spray formed ultra-high strength Al−Zn−Mg−Cu alloy [J]. Materials Characterization, 2018, 144: 131−140.
[30] ZHENG Ya-ya, LUO Bing-hui, BAI Zhen-hai, HE Chuan. Evolution of the initial recipitation and strengthening mechanism of Al−Mg−Si alloys [J]. Journal of The Minerals, Metals & Materials Society, 2019, 71: 4737−4745.

Al−Mg−Si 合金 U 形型材的组织与力学性能

王向东[1]，刘 雄[1]，丁 浩[1]，剡苏荣[1]，谢紫华[1]，
潘柏清[1]，李永红[1]，潘清林[2]，邓运来[2]，王维裔[2]

1. 株洲中车时代电气有限公司 制造中心，株洲 412001；
2. 中南大学 材料科学与工程学院，长沙 410083

摘 要：通过光学显微镜、扫描电镜、透射电镜、硬度测试和拉伸性能测试等方法，研究热挤压工艺、固溶时效工艺对 Al−Mg−Si 合金 U 形型材组织与性能的影响。结果表明：在热挤压过程中，型材中部分晶粒会发生动态再结晶，再结晶晶粒随后粗化形成粗晶层。在加工硬化和动态回复的共同作用下，粗晶层间的晶粒呈纤维状和亚结构。时效处理后，晶内形成相互垂直的针状 β''相，晶界处可见明显的无沉淀析出带。Al−Mg−Si 合金 U 型型材的抗拉强度、屈服强度、伸长率分别不低于 279.4 MPa、258.6 MPa 和 21.6%，其断口呈韧窝断裂特征。晶界强化和析出强化对型材强度提高有明显贡献。

关键词：Al−Mg−Si 合金；U 形型材；热挤压；显微组织；力学性能；析出相

(Edited by Xiang-qun LI)